Evaluation of the hardness and Young's modulus of electrodeposited Al–W alloy films by nano-indentation

Shota Higashino[1], Masao Miyake[1,*], Ayumu Takahashi[1], Yuya Matamura[1], Hisashi Fujii[1], Ryuta Kasada[2], Tetsuji Hirato[1]

[1:] Graduate School of Energy Science, Kyoto University, Yoshida-honmachi, Sakyo-ku, Kyoto, 606-8501, Japan

[2:] Institute of Advanced Energy, Kyoto University, Gokasho, Uji-shi, Kyoto, 611-0011, Japan

*Corresponding author.

TEL: +81-75-753-5914, E-mail: miyake.masao.4e@kyoto-u.ac.jp

Abstract

Al–W alloy films with various W contents up to ~12 at% were prepared by electrodeposition using 1-ethyl-3-methylimidazolium chloride (EMIC)–$AlCl_3$ ionic liquids with different concentrations of W precursor, W_6Cl_{12}. The hardness (*H*) and Young's modulus (*E*) of the films were examined by nano-indentation. The films were composed of a single-phase fcc Al super-saturated solid solution, an amorphous phase, or both, depending on the W content and the deposition conditions. The *H* value increased with increasing W content up to 9.8 at% and then decreased slightly with further increases in the W content up to 12.4 at%. A similar trend was observed in the *E* value with increasing W content, but the decrease in *E* value at 12.4 at% W was more significant than that in *H* value. The changes in the *H* and *E* values are discussed from the viewpoints of the grain size and the constituent phases. The 9.8–12.4 at% W films, which had relatively high *H* values and *H*/*E* ratios, are expected to have a higher resistance to mechanical damage than Al films.

Keywords

Electroplating, Ionic liquid, Nano-indentation, Amorphous alloy, Aluminum, Tungsten

1. Introduction

Al metal shows high oxidation and corrosion resistance because of the thin passive film on its surface. Thus Al metal films have attracted much research attention as corrosion-protective coatings on reactive materials such as a Mg alloy [1,2]. However, if exposed to an environment containing halide anions such as Cl^-, the passive film on Al metal is destroyed locally, followed by pitting corrosion [3]. The resistance of Al metal to pitting corrosion is enhanced by alloying with other transition metals [3]. Among Al alloys, Al–W alloys are known to exhibit significant resistance to pitting corrosion [3,4]. Therefore, the formation of Al–W alloy films was intensively studied.

The formation of Al–W alloy films by sputtering [4–15], ion implantation [16], laser surface alloying [17], and electrodeposition [18–22] was reported. Of these methods, electrodeposition has particular advantages in that a thick film can be formed over a large area relatively quickly by means of simple equipment. The electrodeposition of Al–W alloys with high W contents was achieved using a 1-ethyl-3-methylimidazolium chloride (EMIC)–$AlCl_3$ ionic liquid containing potassium tungsten(III) chloride, $K_3W_2Cl_9$ [18–20]. However, alloys with more than 5 at% W obtained from this bath showed a powdery morphology. The morphology was improved by changing the W precursor from $K_3W_2Cl_9$ to tungsten(II) chloride, W_6Cl_{12} [22]. We reported that dense Al–W alloy films with up to ~12 at% W can be electrodeposited from an EMIC–$AlCl_3$ ionic liquid containing W_6Cl_{12} [22]. The Al–W alloy films obtained from this bath were composed of a super-saturated fcc Al solid solution with W contents lower than ~9 at%, and with an amorphous phase of higher W content.

When Al–W alloy films are employed as corrosion-protective coatings, the mechanical strength of the films is also an important factor to consider. In particular, if the film is applied onto a reactive material such as a Mg alloy, mechanical damage penetrating through the film can cause galvanic corrosion of the base material [23]. To avoid such

corrosion, the film needs to have a high mechanical strength. However, the data on the mechanical properties of Al–W alloy films are limited. A few reports on the Vickers hardness of sputtered Al–W alloy films are available in the literature [10,15]. According to the reports [10,15], the hardness increases from 1.7 GPa for an Al–0.6 at% W alloy to 20 GPa for an Al–50 at% W alloy. No data for electrodeposited films were published except for the hardness and Young's modulus of the Al–12 at% W amorphous alloy reported in our previous study [22]. The mechanical properties of the alloy films depend on their composition, constituting phase, grain size, and process conditions. However, such details were not elucidated for the electrodeposited Al–W alloy films. In this study, films with different W contents and different phases were prepared by electrodeposition using EMIC–$AlCl_3$ ionic liquids at several W_6Cl_{12} concentrations. The hardness and Young's modulus of the resulting films were measured by nano-indentation. The effects of W content, phase, and grain size on the hardness and Young's modulus are discussed.

2. Material and methods

The electrolytic bath was prepared by adding anhydrous aluminum chloride ($AlCl_3$, 99%, Fluka) to EMIC (97%, Tokyo Chemical Industry) at a molar ratio of 2:1. The EMIC was dried under vacuum at 120°C prior to use. The W precursor, W_6Cl_{12}, was synthesized by a modified method [22] similar to that described in the literature [24,25].

Electrochemical experiments using the EMIC–$AlCl_3$–W_6Cl_{12} baths were carried out in an argon-filled glove box (UN-800F, UNICO) equipped with a circulation system (CM-200, UNICO). A glass vessel with a volume of 25 mL was used as an electrolytic cell. The bath temperature was kept at 80°C by a heater and thermostat (TJA-550, AS ONE) connected to a rubber heater wound around the cell and a thermocouple soaked in the bath.

Galvanostatic electrodeposition was performed on a polished Ni plate. A section of the Ni plate was covered with polytetrafluoroethylene tape so to expose a defined area (5 mm × 5 mm). An Al plate was used as the counter electrode. The Ni plate and Al plate were

placed vertically and in parallel to each other. The distance between the Ni and Al plates was less than 10 mm. During the electrodeposition process, the bath was agitated at 150 rpm using a magnetic stirrer (PC-420D, CORNING) and a magnetic flea (15 mm × 5 mm). The electrochemical experiments described above were carried out using an electrochemical analyzer (HZ-5000, Hokuto Denko). After the electrodeposition, the deposit was washed with distilled water and ethanol.

A scanning electron microscope (SEM, JEOL, JSM-6510LV) combined with energy dispersive X-ray spectroscopy (EDX, INCAx-act, Oxford Instruments) was employed to observe the morphology and measure the elemental composition of the deposit. X-ray diffraction (XRD) patterns were obtained with an X-ray diffractometer (X'pertPRO-MPD, PANalytical) under Cu Kα radiation (λ = 0.15405 nm).

The hardness and Young's modulus of the Al–W alloy films were determined by nano-indentation tests using a nano-indenter (G200, Agilent Technologies) with a diamond Berkovich tip. The surfaces of the electrodeposited 10-μm thick pure Al and Al–W alloy films were mirror polished prior to the indentation tests to minimize the errors caused by surface roughness. Indentation data were collected with the continuous stiffness measurement technique [26–29] with a vibration frequency of 45 Hz. In each indentation, the hardness and Young's modulus values were obtained at a depth of 200 nm, where the influence of the Ni substrate was not influential. The indentation size effect [30] and the influence of the residual stress caused by polishing were also negligible at this depth. Each value reported for the hardness and Young' s modulus are averages of the values taken at 12 indentation points, which were separated by more than 50 μm in all directions. In the evaluation of the Young's modulus, the Poisson's ratio of the Al–W alloy films was assumed to be 0.3, which is a typical value for metallic materials [31]. The error of the Young's modulus caused by varying Poisson's ratio between 0.2 and 0.4 was within 10% [32]. The Young's modulus of the Al film was calculated using the Poisson's ratio reported for Al (0.34) [33,34].

3. Results and Discussion

3.1. Electrodeposition and composition of the deposits

In order to obtain Al and Al–W alloy films with different W content, galvanostatic electrodeposition was carried out at 20 mA cm^{-2} in EMIC–$AlCl_3$ baths containing 0–49 mM W_6Cl_{12}. The amount of charge was set at 30 C cm^{-2}, which corresponds to the value required to electrodeposit a 10.4-μm-thick pure Al film or a 14.8-μm-thick pure W film. Every electrodeposition cycle in the 0–49 mM W_6Cl_{12} baths yielded a whitish-gray film on the Ni substrate. Fig. 1 reports the typical EDX spectra of the deposits, showing that the deposit was composed only from Al and W. No other element was detected, except for a slight amount of O owing to surface oxidation. The W content of the deposits determined by EDX is plotted against the W_6Cl_{12} concentration in Fig. 2, where only the Al and W presence was taken into account. The W content increases with increasing W_6Cl_{12} concentration, reaching 12.4 at% when the W_6Cl_{12} concentration is 24 mM. When the W_6Cl_{12} concentration is higher than 24 mM, the W content is almost constant between 12 and 13 at%. The behavior of the W content with respect to the W_6Cl_{12} concentration is similar to the Langmuir type adsorption isotherm, suggesting that the electrodeposition of W_6Cl_{12} to W(0) occurs via adsorption of W(II) ions on the cathode surface. It can be inferred that the reduction process of the adsorbed W(II) ions to W(0) is slow, and therefore, the number of the W(II) ions adsorbed on the cathode surface is nearly in equilibrium with the W_6Cl_{12} concentration during the electrodeposition. Saturation of W content of the electrodeposited alloy would be due to the saturated adsorption site of W(II) ions on the cathode surface at the bulk W_6Cl_{12} concentration of > 24 mM.

3.2. Morphology

Surface and cross-sectional SEM images of the Al film and the Al–W alloy films are shown in Fig. 3. The 0–9.8 at% W films obtained from the 0–20 mM W_6Cl_{12} baths are composed of angular grains. The grain size of the 0–7.2 at% W films increases with the increase of the W content from ~3 μm for the 0 at% W film to ~10 μm for the 7.2 at% W film, although smaller grains (< 3 μm) are also present in the 7.2 at% W film. The 9.8 at% W film is composed of grains smaller than those observed in the 7.2 at% film. The films with 12–13 at% W obtained from the baths containing more than 24 mM W_6Cl_{12} (Figs. 3f and g) are composed of rounded nodules with diameters less than 10 μm. Grains with crystallographic facets are not observed in these films. The cross-sectional image of the 12.4 at% W film obtained from the 49 mM W_6Cl_{12} bath shows that the film is dense and has good adhesion to the substrate. The average thickness is ~11 μm, which is in agreement with the value estimated from the electric charge.

3.3. Phase identification

The XRD patterns of the Al and Al–W alloy films are shown in Fig. 4. The films with 0–7.2 at% W show characteristic diffraction patterns for fcc Al. The 9.8 and 12.4 at% W films from the 20 and 24 mM W_6Cl_{12} baths show weak fcc Al peaks and a halo around $2\theta = 42°$. The 12–13 at% W films from the baths containing more than 32 mM W_6Cl_{12} show only the halo around $2\theta = 42°$.

An enlarged view of the Al(111) diffraction peaks is shown in the right-hand graph in Fig. 4. The Al(111) peak position shifts to a higher angle with the increase of the W content. These peak shifts indicate the formation of a substitutional solid solution of fcc Al containing W atoms, which have a smaller radius than the Al atoms. According to the Al–W binary phase diagram, the maximum solubility of W in fcc Al phase is 0.022 at% at 640°C [35]. Therefore, the 2.0–12.4 at% W films from the 2–24 mM W_6Cl_{12} baths comprise a super-saturated solid solution of fcc Al phase. The 2.0–7.2 at% W films show only the distinctive diffraction pattern for fcc Al, indicating that these films are mainly

composed of the fcc solid solution. The 9.8 and 12.4 at% W films from the 20 and 24 mM W_6Cl_{12} baths show the diffraction pattern for fcc Al and a halo around $2\theta = 42°$, indicating that the fcc Al solid-solution phase coexists with an amorphous phase. The halo is more evident in the 12.4 at% W film than in the 9.8 at% W film, and therefore the volume fraction of the amorphous phase is higher in the 12.4 at% W film than in the 9.8 at% W film. The 12–13 at% W films from the baths containing more than 32 mM W_6Cl_{12}, showing only the broad halo, should be composed of a single amorphous phase.

The lattice parameters of the fcc Al phase in the 0–12.4 at% W films were calculated from the peak positions of Al(111) based on Bragg's law. In this calculation, the Ni(111) peak position of the Ni substrate was employed as the internal standard. The aluminum lattice parameter (a_{Al}) is plotted against W content in Fig. 5. The value of a_{Al} decreases linearly with increasing W content at 0–7.2 at% W. When the W contents are 9.8 and 12.4 at% W, however, the value of a_{Al} is greater than that expected from the linear relationship seen for 0–7.2 at% W (solid line in Fig. 5). This indicates that some of the W atoms in the 9.8 and 12.4 at% W films are not involved in the fcc Al phase and form the amorphous Al–W alloy phase.

As shown in Figs. 4f and g, even though the W contents are almost the same at around 12–13 at%, the film from the 24 mM W_6Cl_{12} bath is composed of fcc and amorphous phases, whereas those from the higher W_6Cl_{12} concentration baths are composed of a single amorphous phase. This fact indicates that, besides the W content, the W_6Cl_{12} concentration affects the formation of the amorphous phase. Similar observations were reported for several alloys electrodeposited from aqueous solutions [36,37]. According to the explanations given in these reports [36,37], ions adsorbed on the electrode surface prevent the surface diffusion of adatoms and their incorporation into the crystal lattice. Therefore, an amorphous phase tends to be formed in a bath with a higher ion concentration. The formation of the single amorphous phase in higher W_6Cl_{12} concentration baths can be explained by the same mechanism.

The formation of a super-saturated solid solution and the transition to the amorphous phase at a higher W content were also observed in previous studies [5,20,22]. The same trend was also been reported for electrodeposited Al–Mn alloy films [38].

3.4. Hardness and Young's modulus

The hardness (*H*) and Young's modulus (*E*) of the electrodeposited Al and Al–W alloy films were determined by nano-indentation. In Fig. 6a, the *H* values of these films are plotted with solid symbols against the W content. The *H* value increases with increasing W content up to 9.8 at% but decreases with a further increase in the W content to 12.4 at%. This trend is described in more detail in relation to the phase. In films comprising the fcc single phase (0–7.2 at% W), the *H* value monotonically increases with increasing W content. Further increases in the *H* value are observed by the transition from the fcc single phase to the fcc and amorphous phases. However, an increase in the W content in the two-phase region (9.8–12.4 at% W) decreases the *H* value. The *H* value of the single amorphous film is almost the same within the error as that of the two-phase film with the same W content (12.4 at%).

As shown in Fig. 6a, a comparison with the data reported for electrodeposited Al–Mn alloy films reveals that the *H* values at the same solute (W or Mn) content and the behavior of the *H* values depending on the phase are almost the same in the Al–W and Al–Mn alloy films. This fact suggests that the strengthening mechanisms are basically the same in both cases. In the 0–7.2 at% W crystalline films, the increase in *H* value can be attributed to the effects of solution strengthening. Although grain refinement (the Hall–Petch effect) also accounts for the increase in *H* values in the electrodeposited Al–Mn films, it is ruled out in the present case because a decrease in the grain size with increasing W content is not observed in 0–7.2 at% W films by SEM (Figs. 3a–d) and XRD; the full width at half maximum (FWHM) of the Al(111) XRD peak for these films is almost constant regardless of the W content (the right-hand graph in Fig. 4). According to the report on

electrodeposited Al–Mn alloy films [38], the strengthening of the two-phase films is attributed to their microstructure, where fine crystal grains are dispersed in an amorphous matrix, and explained in the manner well known for amorphous metals containing nanocrystals [39,40]. It is suggested that the decrease in the *H* value with increasing Mn content in this two-phase region is caused by a decreasing volume fraction of the reinforcing crystalline phase. The same explanation can be applied to the high *H* values of the 9.8 and 12.4 at% W two-phase films. The grain refinement of these films is confirmed by the SEM images (Figs. 3e and f) and the fact that the FWHM of the XRD peak is larger for the two-phase films than for the 0–7.2 at% W films (the right-hand graph in Fig. 4). The decrease in *H* value with increasing W content from 9.8 to 12.4 at% W is reasonable in terms of the decreasing volume fraction of the crystalline phase, as evidenced by XRD.

The *H* values for the electrodeposited Al–W films are lower by ~2 GPa than the values reported for sputtered Al–W alloy films with similar W contents [15]. The lower values are probably because the grain size of the fcc phase is larger in the electrodeposited films.

Figure 6b shows the *E* values of the films. The *E* value of the Al film (78±4 GPa) was slightly higher than the value reported in literature of 70 GPa [33,34], which was determined by the pulsed ultrasonic method, but close to the value (75–80 GPa) determined by nano-indentation by other research groups [41,42]. Radvic et al. demonstrated that the *E* value of an Al alloy determined by nano-indentation is slightly higher than that determined by other techniques such as resonant ultrasound microscopy, impulse excitation, and four-point bending [43]. The higher value by nano-indentation is ascribed to material pile-up around the indenter tip during the indentation test [44].

As is shown in Fig. 6b, the trend of the change in the *E* value with W content is similar to that in the *H* value, but the decrease in the *E* value from 9.8 to 12.4 at% W is larger than that in the *H* value.

The increase in *E* value with increasing W content in the 0–7.2 at% W films is attributed to stiffer interatomic bonding caused by solute W atoms. In general, the stiffness of interatomic bonding increases with decreasing interatomic distance [31,45,46]. In the 0–7.2 at% W films, solute W atoms decrease the interatomic distance, as evidenced by the decrease in the value of a_{Al} (Fig. 5). The drastic decrease in *E* values at 12.4 at% W is attributed to the amorphous phase. The interatomic distance in amorphous alloys is slightly larger than in their crystalline counterparts, and therefore, in elastic deformation of amorphous alloys, each atom experiences larger displacements that cannot be prescribed by the macroscopic strain, leading to lower *E* values [47,48].

In general, hard materials exhibit a high resistance to mechanical damages. Furthermore, Leyland et al. suggested that materials with a high ratio of hardness to Young's modulus (*H*/*E)* exhibit a high wear resistance [49,50]. The *H*/*E* ratios of the electrodeposited 0–12.4 at% W films are shown in Fig. 6c. The *H*/*E* ratio increases with increasing W content, and the 9.8–12.4 at% W films show a relatively high *H*/*E* ratio of 0.03–0.05. These alloy films, which have relatively high *H* values and *H*/*E* ratios, can be expected to have a higher resistance to mechanical damage than Al films.

4. Conclusion

The electrodeposited Al–W alloy films were composed of a super-saturated fcc Al solid solution phase when the W content was lower than ~9 at%, and an amorphous phase was formed with higher W contents. The hardness (*H*) and Young's modulus (*E*) of the electrodeposited Al–W alloy films with 0–12.4 at% W were measured by nano-indentation. The *H* value increased with increasing W content up to 9.8 at% but then decreased slightly with a further increase in the W content to 12.4 at%. A similar trend is observed for the change in the *E* value. These changes in *H* and *E* values can be explained

by the structural behavior. The 9.8–12.4 at% W films exhibited relatively high *H* values and *H*/*E* ratios, and therefore these films are expected to have a higher resistance to mechanical damage than Al films.

Acknowledgments

We thank Professor T. Doi (Kyoto University) for the SEM and EDX. This work was supported by JSPS KAKENHI grant Number 25630327, and the “Joint Usage/Research Program on Zero-Emission Energy Research, Institute of Advanced Energy, Kyoto University (ZE28-C-7)”.

References

[1] J.E. Gray, B. Luan, Protective coatings on magnesium and its alloys — a critical review, J. Alloys Compd. 336 (2002) 88–113.

[2] G. Song, Recent progress in corrosion and protection of magnesium alloys, Adv. Eng. Mater. 7 (2005) 563–586.

[3] Z. Szklarska-Smialowska, Pitting corrosion of aluminum, Corros. Sci. 41 (1999) 1743–1767.

[4] B.A. Shaw, T.L. Fritz, G.D. Davis, W.C. Moshier, The Influence of Tungsten on the Pitting of Aluminum Films, J. Electrochem. Soc. 137 (1990) 1317–1318.

[5] B.A. Shaw, G.D. Davis, T.L. Fritz, B.J. Rees, W.C. Moshier, The Influence of Tungsten Alloying Additions on the Passivity of Aluminum, J. Electrochem. Soc. 138 (1991) 3288–3295.

[6] G.D. Davis, B.A. Shaw, B.J. Rees, M. Ferry, Mechanisms of passivity of nonequilibrium Al-W alloys, J. Electrochem. Soc. 140 (1993) 951–959.

[7] A. Wolowik, M. Janik-Czachor, Z. Werner, Stability of the passive state of Al-W sputter deposited amorphous alloys, Mater. Chem. Phys. 49 (1997) 164–168.

[8] A. Wolowik, M. Janik-Czachor, Anodic behaviour of Al-refractory metal amorphous alloys, Mater. Sci. Eng. A. 267 (1999) 301–306.

[9] N. Radić, A. Tonejc, M. Milun, P. Pervan, J. Ivkov, M. Stubičar, Preparation and structure of AlW thin films, Thin Solid Films. 317 (1998) 96–99.

[10] M. Stubicar, A. Tonejc, N. Radic, Microhardness characterization of Al-W thin films, Vacuum. 61 (2001) 309–316.

[11] M. Metikos-Hukovic, N. Radic, Z. Grubac, A. Tonejc, The corrosion behavior of sputter-deposited aluminum-tungsten alloys, Electrochim. Acta. 47 (2002) 2387–2397.

[12] J. Ivkov, N. Radić, A. Tonejc, Hall effect in Al-W thin films, Solid State Commun. 129 (2004) 369–373.

[13] J. Ivkov, N. Radić, A. Tonejc, T. Car, Structural relaxation of Al-W amorphous thin films, J. Non. Cryst. Solids. 319 (2003) 232–240.

[14] D.K. Merl, P. Panjan, J. Kovač, Corrosion and surface study of sputtered Al-W coatings with a range of tungsten contents, Corros. Sci. 69 (2013) 359–368.

[15] D.K. Merl, P. Panjan, I. Milošev, Effect of tungsten content on properties of PVD sputtered Al–Wx alloys, Surf. Eng. 29 (2013) 281–286.

[16] C.M. Rangel, M.A. Travassos, J. Chevallier, Microstructural modifications of aluminium surfaces ion implanted with W and its effect on corrosion and passivation, Surf. Coat. Technol. 89 (1997) 101–107.

[17] R.S. Rajamure, H.D. Vora, S.G. Srinivasan, N.B. Dahotre, Laser alloyed Al-W coatings on aluminum for enhanced corrosion resistance, Appl. Surf. Sci. 328 (2015) 205–214.
[18] T. Tsuda, C.L. Hussey, G.R. Stafford, Progress in Surface Finishing with Lewis Acidic Room-Temperature Chloroaluminate Ionic Liquids, ECS Trans. 3 (2007) 217–231.
[19] T. Tsuda, Y. Ikeda, T. Arimura, A. Imanishi, S. Kuwabata, C.L. Hussey, G.R. Stafford, Al-W Alloy Deposition from Lewis Acidic Room-Temperature Chloroaluminate Ionic Liquid, ECS Trans. 50 (2012) 239–250.
[20] T. Tsuda, Y. Ikeda, T. Arimura, M. Hirogaki, A. Imanishi, S. Kuwabata, G.R. Stafford, C.L. Hussey, Electrodeposition of Al-W Alloys in the Lewis Acidic Aluminum Chloride-1-Ethyl-3-Methylimidazolium Chloride Ionic Liquid, J. Electrochem. Soc. 161 (2014) D405–D412.
[21] K. Sato, H. Matsushima, M. Ueda, Electrodeposition of Al-W alloys in $AlCl_3$-NaCl-KCl molten salt containing WCl_4, ECS Trans. 75 (2016) 305–312.
[22] S. Higashino, M. Miyake, H. Fujii, A. Takahashi, T. Hirato, Electrodeposition of Al-W Alloy Films in a 1-Ethyl-3-methyl-imidazolium Chloride-$AlCl_3$ Ionic Liquid Containing W_6Cl_{12}, J. Electrochem. Soc. 164 (2017) D120–D125.
[23] G. Song, B. Johannesson, S. Hapugoda, D. StJohn, Galvanic corrosion of magnesium alloy AZ91D in contact with an aluminium alloy, steel and zinc, Corros. Sci. 46 (2004) 955–977.
[24] V. Kolesnichenko, L. Messerle, Facile Reduction of Tungsten Halides with Nonconventional, Mild Reductants. 2. Four Convenient, High-Yield Solid-State Syntheses of the Hexatungsten Dodecachloride Cluster W_6Cl_{12} and Cluster Acid $(H_3O)_2[W_6(\mu_3\text{-}Cl)_8Cl_6](OH_2)_x$, Including New Cation-Assisted , Inorg. Chem. 37 (1998) 3660–3663.
[25] M. Strobele, T. Justel, H. Bettentrup, H.-J. Meyer, The synthesis and Luminescence of W_6Cl_{12} and Mo_6Cl_{12} revisited, Z. Anorg. Allg. Chem. 635 (2009) 822–827.
[26] W.C. Oliver, G.M. Pharr, An improved technique for determining hardness and elastic modulus using load and displacement sensing indentation experiments, J. Mater. Res. 7 (1992) 1564–1583.
[27] W.C. Oliver, G.M. Pharr, Measurement of hardness and elastic modulus by instrumented indentation: Advances in understanding and refinements to methodology, J. Mater. Res. 19 (2004) 3–20.
[28] X. Li, B. Bhushan, A review of nanoindentation continuous stiffness measurement

technique and its applications, Mater. Charact. 48 (2002) 11–36.
[29] J. Hay, P. Agee, E. Herbert, Continuous stiffness measurement during instrumented indentation testing, Exp. Tech. 34 (2010) 86–94.
[30] G.M. Pharr, E.G. Herbert, Y. Gao, The Indentation Size Effect: A Critical Examination of Experimental Observations and Mechanistic Interpretations, Annu. Rev. Mater. Res. 40 (2010) 271–292.
[31] T. Rouxel, Elastic properties and short-to medium-range order in glasses, J. Am. Ceram. Soc. 90 (2007) 3019–3039.
[32] P.K. Zysset, X. Edward Guo, C. Edward Hoffler, K.E. Moore, S.A. Goldstein, Elastic modulus and hardness of cortical and trabecular bone lamellae measured by nanoindentation in the human femur, J. Biomech. 32 (1999) 1005–1012.
[33] D. Lazarus, The variation of the Adiabatic Elastic Constants of KCl, NaCl, CuZn, Cu, and Al with Pressure to 10,000 Bars, Phys. Rev. 76 (1949) 545–553.
[34] G. Simmons, H. Wang, Single Crystal Elastic Constants and Calculated Aggregate Properties: A Handbook, 2nd ed, The M.I.T. Press, Cambridge, MA, 1971.
[35] S.V.N. Naidu, P.R. Rao, eds., Phase Diagrams of Binary Tungsten Alloys, Indian Institute of metals, Calcutta, 1991.
[36] Y. Fukunaka, S. Aikawa, Z. Asaki, Fundamental Study on Electrodeposition of Co and Co-P Films, J. Electrochem. Soc. 141 (1994) 1783–1791.
[37] T. Burchardt, V. Hansen, T. Våland, Microstructure and catalytic activity towards the hydrogen evolution reaction of electrodeposited NiPx alloys, Electrochim. Acta. 46 (2001) 2761–2766.
[38] S. Ruan, C.A. Schuh, Electrodeposited Al-Mn alloys with microcrystalline, nanocrystalline, amorphous and nano-quasicrystalline structures, Acta Mater. 57 (2009) 3810–3822.
[39] Y.H. Kim, A. Inoue, T. Masumono, Ultrahigh Tensile Strength of $Al_{88}Y_2Ni_9M_1$ (M=Mn or Fe) Amorphous Alloys Containing Finely Dispersed fcc-Al Particles, Mater. Trans. 31 (1990) 747.
[40] A. Inoue, H. Kimura, Fabrications and mechanical properties of bulk amorphous, nanocrystalline, nanoquasicrystalline alloys in aluminum-based system, J. Light Met. 1 (2001) 31–41.
[41] Z. Lee, C. Ophus, L.M. Fischer, N. Nelson-Fitzpatrick, K.L. Westra, S. Evoy, V. Radmilovic, U. Dahmen, D. Mitlin, Metallic NEMS components fabricated from nanocomposite Al-Mo films, Nanotechnology. 17 (2006) 3063–3070.
[42] S. Varam, K. V. Rajulapati, K. Bhanu Sankara Rao, Strain rate sensitivity studies on bulk nanocrystalline aluminium by nanoindentation, J. Alloys Compd. 585

(2014) 795–799.
[43] M. Radovic, E. Lara-Curzio, L. Riester, Comparison of different experimental techniques for determination of elastic properties of solids, Mater. Sci. Eng. A. 368 (2004) 56–70.
[44] T.Y. Tsui, G.M. Pharr, Substrate effects on nanoindentation mechanical property measurement of soft films on hard substrates, J. Mater. Res. 14 (1999) 292–301.
[45] J.G. Wang, B.W. Choi, T.G. Nieh, C.T. Liu, Crystallization and nanoindentation behavior of a bulk Zr–Al–Ti–Cu–Ni amorphous alloy, J. Mater. Res. 15 (2000) 798–807.
[46] C.C. Yuan, X.K. Xi, On the correlation of Young's modulus and the fracture strength of metallic glasses, J. Appl. Phys. 109 (2011) 33515.
[47] C.A. Schuh, T.C. Hufnagel, U. Ramamurty, Mechanical behavior of amorphous alloys, Acta Mater. 55 (2007) 4067–4109.
[48] D. Weaire, M.F. Ashby, J. Logan, M.J. Weins, On the use of pair potentials to calculate the properties of amorphous metals, Acta Metall. 19 (1971) 779–788.
[49] A. Leyland, A. Matthews, On the significance of the H/E ratio in wear control: A nanocomposite coating approach to optimised tribological behaviour, Wear. 246 (2000) 1–11.
[50] A. Leyland, A. Matthews, Design criteria for wear-resistant nanostructured and glassy-metal coatings, Surf. Coat. Technol. 177–178 (2004) 317–324.

Figure Captions

Fig. 1 EDX spectrum of the electrodeposited film at 20 mA cm^{-2} in an EMIC–$AlCl_3$ bath containing 49 mM W_6Cl_{12}.

Fig. 2 W content of Al–W alloy films electrodeposited at 20 mA cm^{-2} in EMIC–$AlCl_3$ baths containing 0–49 mM W_6Cl_{12}.

Fig. 3 (a–g) Surface and (h) cross-sectional SEM images of Al and Al–W alloy films obtained from EMIC–$AlCl_3$ baths containing 0–49 mM W_6Cl_{12}. The W_6Cl_{12} concentration and the W content of the films are (a) 0 mM, 0 at%, (b) 4 mM, 2.0 at%, (c) 8 mM, 5.0 at%, (d) 16 mM, 7.2 at%, (e) 20 mM, 9.8 at%, (f) 24 mM, 12.4 at%, and (g, h) 49 mM, 12.4 at%

Fig. 4 (Left) XRD patterns of Al and Al–W alloy films obtained from EMIC–$AlCl_3$ baths containing 0–49 mM W_6Cl_{12}. The W_6Cl_{12} concentration and the W content of the films are: (a) 0 mM, 0 at%, (b) 4 mM, 2.0 at%, (c) 8 mM, 5.0 at%, (d) 16 mM, 7.2 at%, (e) 20 mM, 9.8 at%, (f) 24 mM, 12.4 at%, and (g) 49 mM, 12.4 at%. The arrows indicate the diffraction peaks from the Ni substrate. The peak positions for fcc Al (ICDD: 00-004-0787) are shown at the top of the figure. (Right) An enlarged view of the Al(111) diffraction peaks of the films.

Fig. 5 Lattice parameter of fcc Al phase in Al and Al–W alloy films obtained from EMIC–$AlCl_3$ baths containing 0–49 mM W_6Cl_{12}.

Fig. 6 (Solid symbols) (a) Hardness (*H*), (b) Young's modulus (*E*), and (c) *H*/*E* ratio of Al and Al–W alloy films electrodeposited from EMIC–$AlCl_3$ baths containing 0–49 mM W_6Cl_{12}. (Open symbols) Hardness of Al and Al–Mn alloy films electrodeposited from EMIC–$AlCl_3$ baths containing 0–200 mM $MnCl_2$ as reported by Ruan and Schuh (2009) [38].

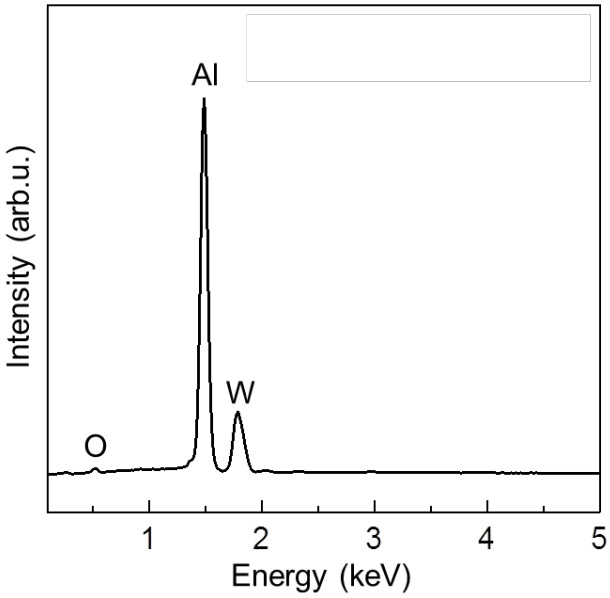

Fig. 1

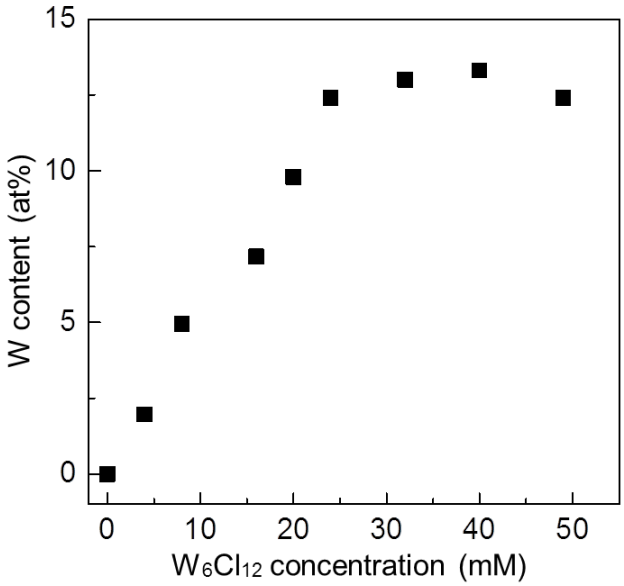

Fig. 2

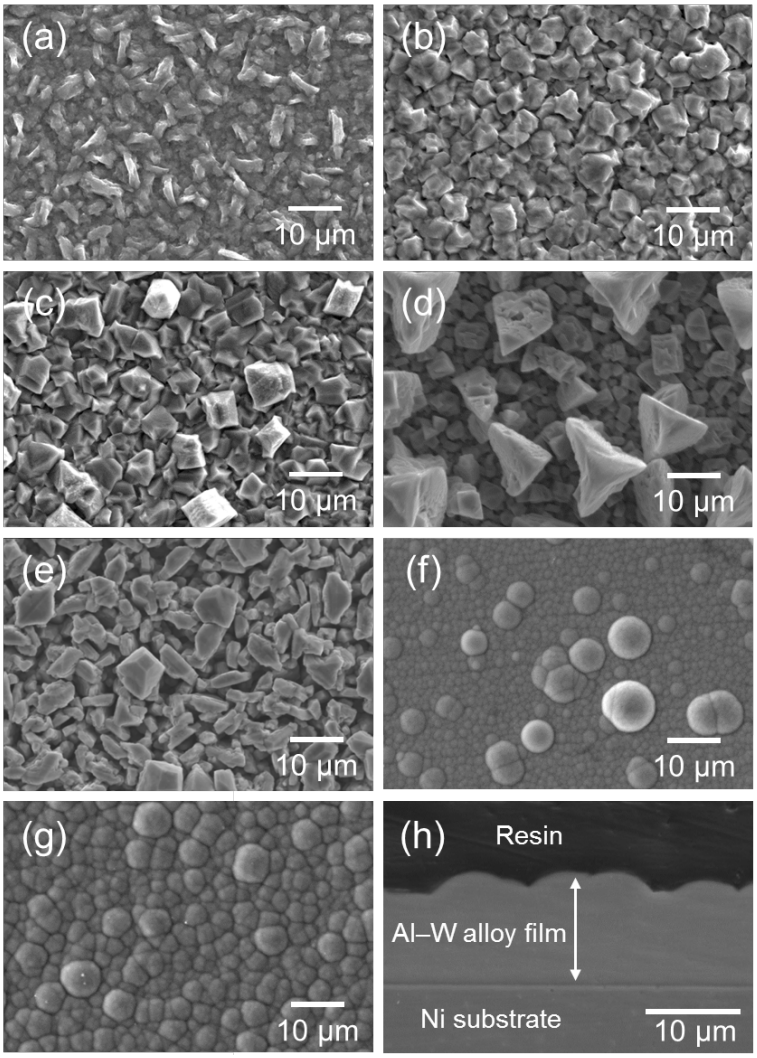
(a)
10 μm
(b)
10 μm
(c)
10 μm
(d)
10 μm
(e)
10 μm
(f)
10 μm
(g)
10 μm
(h)
Resin
Al–W alloy film
Ni substrate
10 μm

Fig. 3

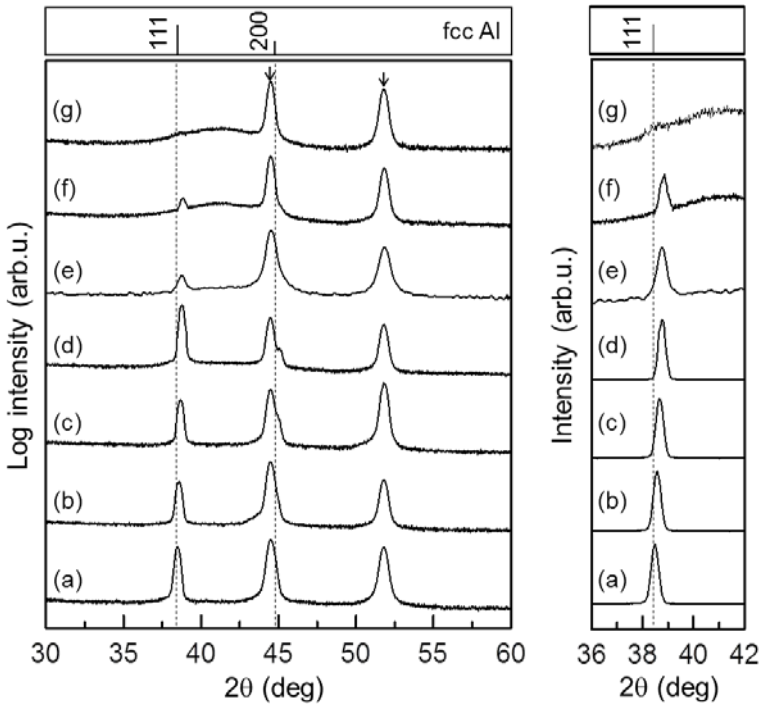
111
200
fcc Al
(g)
(f)
(e)
(d)
(c)
(b)
(a)
Log intensity (arb.u.)
30 35 40 45 50 55 60
2θ (deg)
111
Intensity (arb.u.)
36 38 40 42
2θ (deg)

Fig. 4

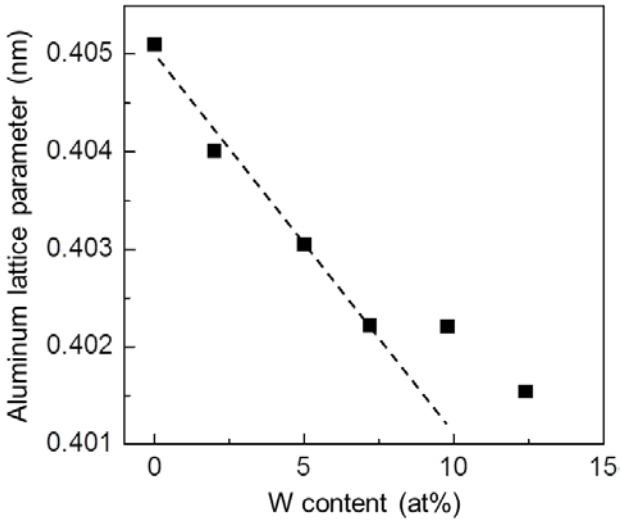
Aluminum lattice parameter (nm)
0.405
0.404
0.403
0.402
0.401
0
5
10
15
W content (at%)

Fig. 5

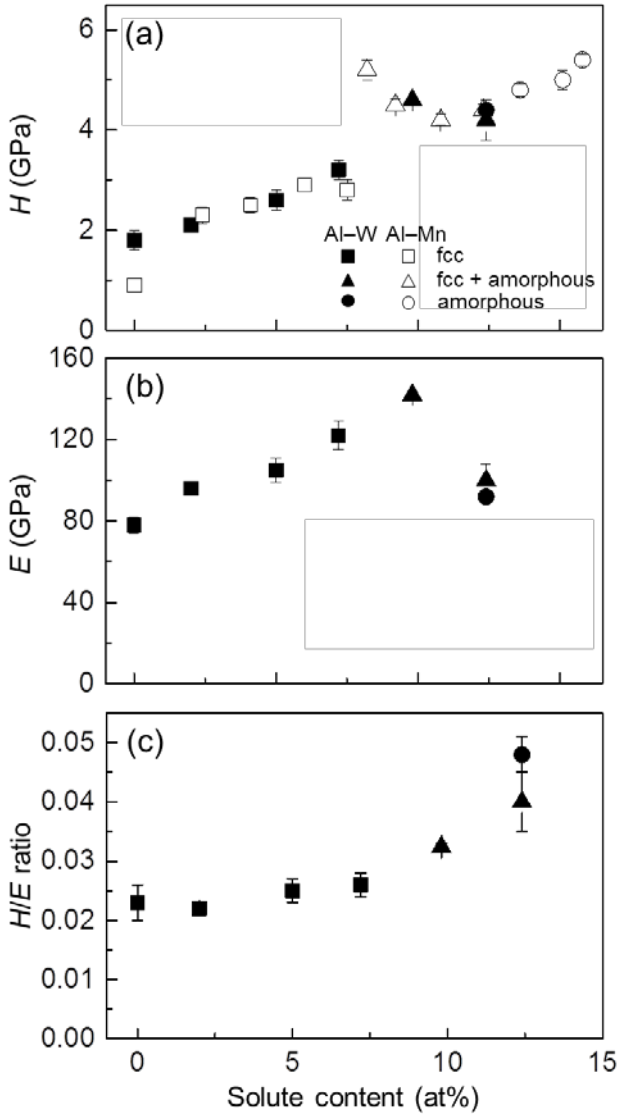
(a)
H (GPa)
Al–W Al–Mn
fcc
fcc + amorphous
amorphous
(b)
E (GPa)
(c)
H/E ratio
Solute content (at%)

Fig. 6